Seventeen Antarctic seismic events detected by global surface waves and a possible link to calving events from satellite images

X. Chen,[1] P. M. Shearer,[1] F. Walter,[1] and H. A. Fricker[1]

[1] We detect 17 seismic events in Antarctica from 1997 to 2009 by applying a surface wave detector to global seismic data. We locate these events using a waveform cross-correlation method and find that most occurred near the coast of Antarctica and are clustered in three regions: four events are on the Ronne Ice Shelf, close to the location of a 1998 calving event; five events are near the Vanderford Glacier; and eight events are near the Ninnis Glacier. The observed Rayleigh and Love waves for these events have similar amplitudes and a two-lobed radiation pattern, matching the expected amplitude behavior of a single-force source model. Using such a model, we obtain best fitting horizontal force directions for the 14 events that have relatively better signal-to-noise ratios. Analysis of coastline changes from MODIS images before and after the detected events show that two events on Vanderford Glacier and one event near Ninnis Glacier are likely associated with calving events. Moreover, the inferred force directions for the seismic events appear consistent with local ice flow directions. Both satellite observations and modeling results strongly suggest a link between seismic events and calving processes in the two regions. However, the force directions on the Ronne Ice Shelf are aligned with observed rift propagation directions, suggesting that these events may arise from rifting processes.

1. Introduction

[2] Since the 1970s, glaciologists have found that changes in ice dynamic processes can sometimes be fast enough (i.e., seconds to minutes) to generate seismic waves that can be recorded by seismometers. Previous observations include crevassing events with high frequency (~100 Hz) [*Neave and Savage*, 1970], calving events at frequencies of ~1 to 3 Hz [*O'Neel et al.*, 2007; *Walter et al.*, 2010], and basal micro-seismicity from stagnant ice stream C in west Antarctica [*Anandakrishnan and Alley*, 1997]. Surface wave energy is observed at some regions, such as repeating ice quakes with an excess of surface wave energy from 0.1 to 1 Hz [*Danesi et al.*, 2007], teleseismically observed glacial earthquakes and earthquakes from stick-slip motion of ice streams with significant surface wave energy lower than ~0.5 Hz [*Ekström et al.*, 2003; *Wiens et al.*, 2008].

[3] Most of the reported events have been detected using local seismic networks and generally have magnitudes ranging from −3 to 2.5 [*Walter et al.*, 2009; *Danesi et al.*, 2007]. The glacial earthquakes reported by *Ekström et al.* [2003] were different, however, in that they had larger sizes, indicating larger ice volumes involved in glacier dis-

placement processes, and a relative lack of high frequency energy, which explains why they were missing from traditional catalogs despite equivalent magnitudes of 4.6 to 5.1. *Ekström* [2006] detected glacial earthquakes in Greenland, Alaska and Antarctica from a surface wave detector. *Tsai and Ekström* [2007] focused on events in Greenland, where most of these glacial earthquakes are located. They analyzed 184 events that occurred in Greenland between 1995 and 2005, studied their temporal and spatial distributions as well as their source mechanisms, and found that (1) after relocation, events clustered in outlet glacier regions, indicating they are probably associated with fast ice flow; (2) a centroid single force (CSF) model fits waveforms better than traditional centroid moment tensor (CMT) solutions, indicating that these events are similar to landslides in mechanism, and their force directions are consistent with ice flow directions; (3) the temporal distributions are different in different regions, however, they generally have higher occurring rates in summer, when surface melting occurs. Also in Greenland, detailed satellite images reveal a strong correspondence between glacial earthquakes and ice front retreat, and their occurrence agrees well with seasonal variations of calving rates [*Joughin et al.*, 2008]. *Amundson et al.* [2008] found a correlation between glacial earthquakes and calving events that include overturning icebergs, however, they found no recordable glacial response during glacial earthquakes as suggested by a glacier sliding model [*Tsai et al.*, 2008]. A direct link between calving events, glacial earthquakes and ice flow was established by *Nettles et al.* [2008] and *de Juan*

---

[1]Scripps Institution of Oceanography, University of California, San Diego, La Jolla, California, USA.

et al. [2010] from GPS surveys and seismic records. Thus a variety of different studies now strongly link glacial earthquakes in Greenland with major calving events.

[4] In Antarctica, only a small number of possible glacial earthquakes have been identified. More than 500 seismic events in West Antarctica have been recorded with two Global Seismic Network stations. The magnitudes of these events range from 3.6 to 4.2, with surface wave energy between 20 and 150 s, however, they seem to result from stick-slip motion of Whillans Ice Stream [*Wiens et al.*, 2008]. Furthermore, *Nettles and Ekström* [2010] reported detection of 14 Antarctic events from global surface waves between 1993 and 2008, which locate near the Antarctic coast.

[5] Here, we describe results of applying a surface wave detector to global seismic data from 1997 to 2009. Similar to *Ekström* [2006], we find hundreds of previously uncataloged earthquakes, including many possible glacial events in Greenland, Alaska, and Antarctica. The majority of these events are in Greenland, and many were previously included in the catalog of *Tsai and Ekström* [2007]. We focus our analysis on 17 events detected in Antarctica and compute refined locations using waveform cross correlation. These events are clustered in three regions: (1) the Ronne Ice Shelf, West Antarctica, (2) near Vanderford Glacier, East Antarctica, and (3) near Ninnis Glacier, East Antarctica. We model their generation mechanism with a centroid single-force model similar to that used by *Tsai and Ekström* [2007]. We also compare the computed force directions of the events with local ice flow directions (I. Joughin, personal communication, 2009) obtained from InSAR data [*Joughin*, 2002], deglaciation crustal response [*James and Ivins*, 1995, 1998], rift propagation [*Larour et al.*, 2004; *Rignot and MacAyeal*, 1998] and satellite imaging of possible calving events, to determine the most likely source mechanisms for the events in each region.

2. Seismic Event Detection

[6] Our seismic detection approach is similar to previous surface wave detection methods used by *Shearer* [1994] and *Ekström* [2006], which work by performing a computer search for times and locations of possible events that predict seismic arrivals that match the observations. *Shearer* [1994] collected data from the IDA (International Deployment of Accelerometers) network, stacked seismograms from 564 events ($m\_b \geq 6$) recorded at very long periods ($T \geq 60$ s), and used the first 3 hours of this time versus range image to construct a matched filter. Then using a global grid of candidate earthquake locations, he stacked seismograms with respect to source-receiver range to produce a time versus range function, which he cross correlated with the matched filter to produce peaks of likely events as a function of time and location. Application of this method to 11 years of IDA data from 1981 to 1991 identified 4061 events, including 65% of cataloged events of $m_b \geq 5.5$ and 32 new events. *Ekström* [2006] used LHZ (long-period, high-gain seismometer, vertical component) seismograms from global networks with broadband instrumentation and defined a $4° \times 4°$ grid of points as target locations. At each target location, he deconvolved a propagation operator for each station, and selected stations based on the observed noise level, probable signal

level, and contribution to azimuthal coverage. He then calculated envelope functions, correlated them with a template peak shape, and defined detections by high correlations occurring on multiple stations at the same time. Once an event was detected, the location was refined using a $0.25° \times 0.25°$ grid, a quality grade was assigned, and a magnitude estimated based on the envelope function amplitude. Analysis of data from 1993 to 2003 detected 24,412 events, including 9482 of 10,159 (93.3%) CMT earthquakes and 1301 new events not listed in the PDE (Preliminary Determinations of Epicenters), ISC (International Seismological Center) and REB (Reviewed Event Bulletin) catalogs.

[7] In our approach, we begin by obtaining continuous VHZ (very long-period, high-gain seismometer, vertical component) data archived at the IRIS DMC at a 0.1 Hz sample rate (10 s sample interval). We organize the data into monthly files and band-pass filter the seismograms between 0.014 and 0.028 Hz. We then apply an automatic gain control filter as described by *Shearer* [1991] to normalize the amplitudes by calculating a 2 min short-term average to 15 min long-term average (STA/LTA) ratio. In this way, we discard the polarity information of the data and use envelope functions with positive values only for stacking. We define 1654 $5° \times 5°$ grid points as candidate earthquake locations. The grid points are spaced at approximately equal distance, resulting in increased longitude spacing near the poles. At each target location, we align the envelope functions by source-receiver range and stack them along a predicted Rayleigh wave group velocity travel-time curve, using 3.955 km/s as an approximate value for the globally average group velocity. To provide more uniform global contributions to the stack from regions that may have very different station densities, we weight each trace inversely by the number of traces within $30°$ bins in azimuth and distance from the target event location. The result of this stacking procedure is a function of space (discretized at $5°$ increments) and time (discretized at 10 s intervals) that contains peaks that most likely correspond to seismic events.

[8] We compare the times and locations of these peaks with those of known events in the PDE, ISC and REB catalogs. If the time offset between a peak and an event in the catalog is less than 20 min and the distance offset is less than $20°$, the peak is automatically associated with the catalog event. While this is the case for most of our detections, some of the peaks do not correspond to catalog events. We use a graphical user interface (GUI) tool to plot record sections for unassociated peaks and visually check them to weed out false triggers (e.g., artifacts due to random alignment of noise spikes, second arriving Rayleigh wave misidentified as first arrival, etc.). We also use the GUI to examine cataloged events within a larger spatial and temporal range than used in our automatic association method in order to identify missed associations. Sometimes the occurrence of two or more events at similar times but different locations can confuse our algorithm, and these situations must be handled manually. For the confirmed "new" events, we assign a quality grade (A, B or C), which depends on the coherence and robustness of the signal. Grade A is reserved for obvious events with well-defined arrivals over a wide distance range. Grade B is for weaker, more intermittent arrivals, but where an event is still clearly present. Grade C is for marginal signals where an event is likely but
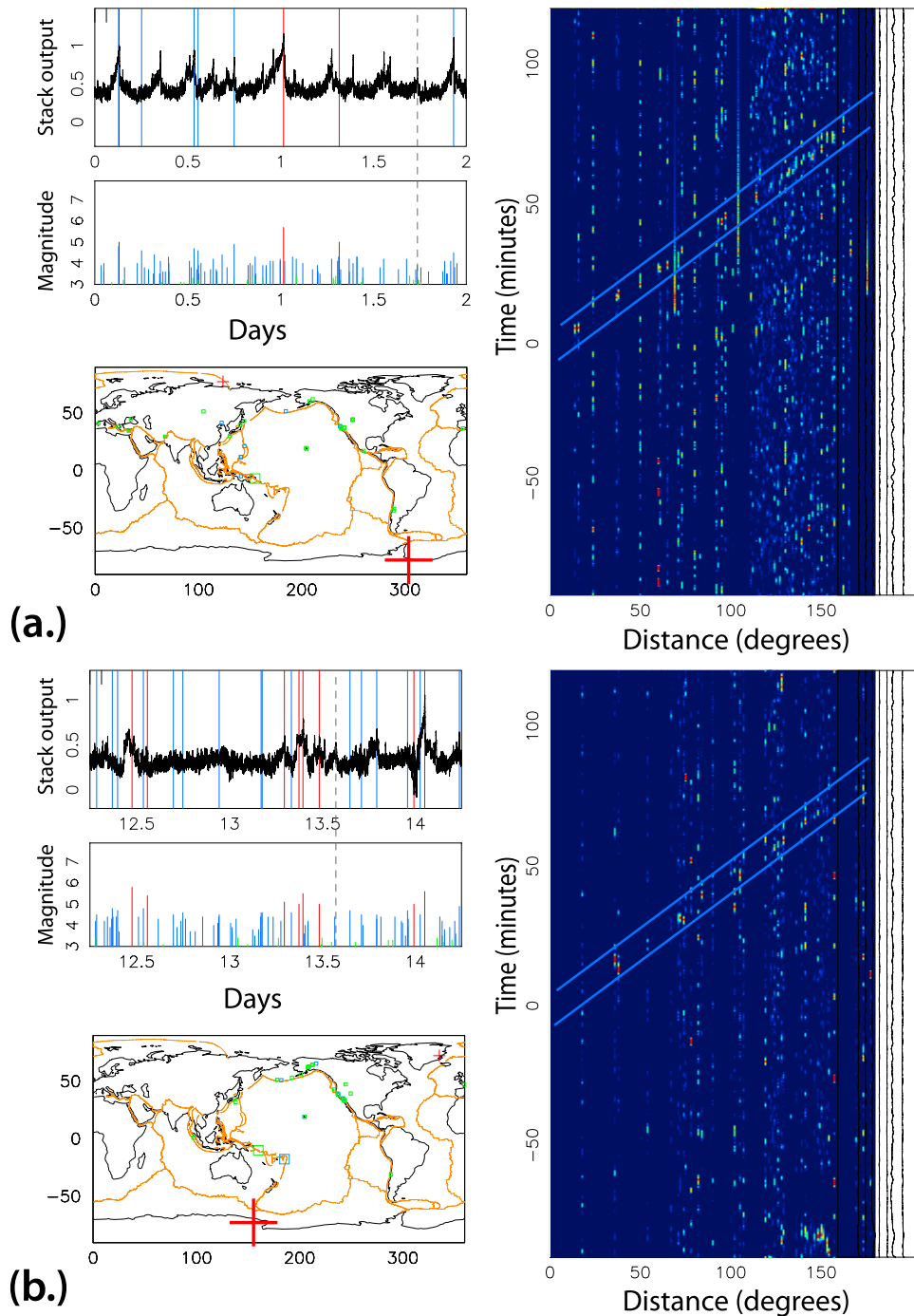
Figure 1. Examples from the GUI display for checking detected events. (a) Grade B event in Antarctica, 2 June 1999; (b) grade C event in Antarctica, 14 May 2007. In both Figures 1a and 1b the upper left panel displays the output of our detector in a 2 day interval, with peaks indicating the times of likely events. The red and blue lines show detected (associated) catalog events of M > 5 and M > 3.5, respectively. The dashed line shows the time of an unassociated peak selected by the user for examination. The right panel shows a record section plot of seismograms for an assumed event at the time of this peak and the best fitting location given by the algorithm, the different colors indicate the amplitude of the stacked seismograms, red means high amplitude while dark means low amplitude. The blue lines indicate the predicted Rayleigh wave arrivals. This location is plotted as the large red cross in the map view, which also shows catalog events within 120 min of the target event as squares (blue means the time offset is less than 30 min, and green means the time offset is between 30 and 120 min). The small red cross shows the target event antipode. The middle left panel shows catalog event magnitudes.
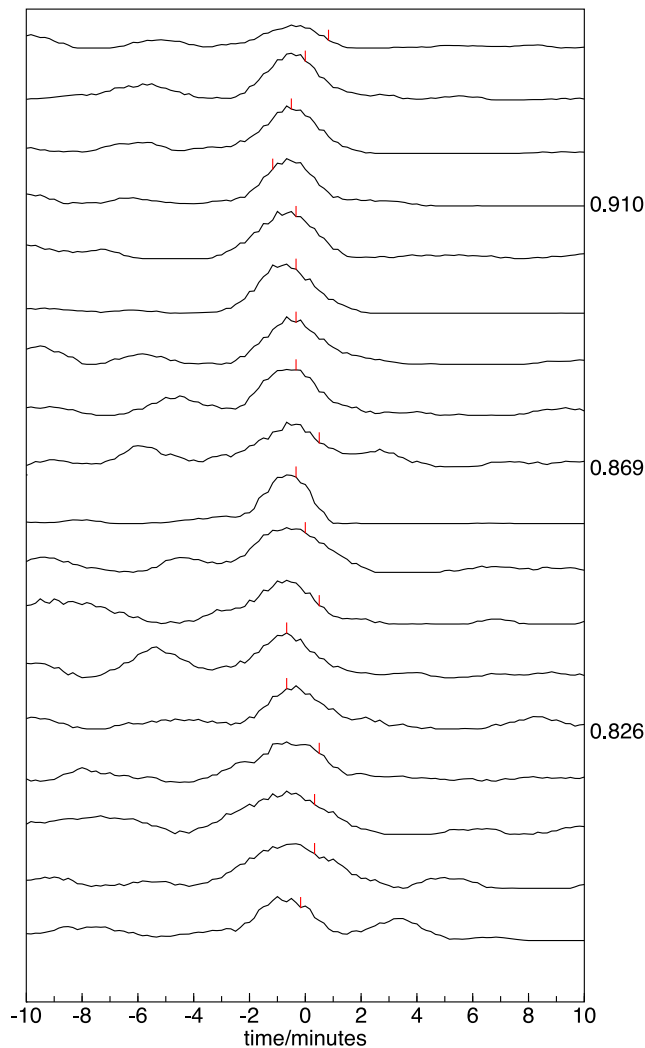
Figure 2. Envelope functions calculated from the STA/LTA filter aligned using our cross-correlation method for an event in Antarctica occurring on 27 June 1999. Red ticks indicate predicted arrival times at the original location. Traces are sorted by correlation coefficient (plotted at right) between the traces and a weighted stack of all the traces (see text).

not conclusively present. Figure 1 shows examples of the GUI output for events assigned Grades B and C in Antarctica.

[9] With this method, we detect 78% of the events in the Global Centroid Moment Tensor (CMT) catalog between 1997 and 2009, and 1100 new events not listed in the PDE, ISC and REB catalogs. Many of these new events were previously detected by *Ekström* [2006] using a similar surface wave detection method. Our analysis here focuses on 17 uncataloged events found in Antarctica (14 grade B and 3 grade C), four of which were also identified by the surface wave detection algorithm described by *Nettles and Ekström* [2010]. These events are clustered into three groups in the following locations: (1) the Ronne Ice Shelf, (2) near Ninnis Glacier, and (3) Vanderford Glacier. Waveforms for events with grade C are generally poorly coherent, with an identifiable signal at very few stations, therefore, our analysis

focuses on the 14 grade B events. We also compute equivalent surface wave magnitudes using the measured amplitudes at 50 s for the grade B events.

3. Relocation

[10] Our initial locations have a nominal accuracy of only 5° (556 km) because they are derived from a coarse grid of candidate locations and a single fixed Rayleigh wave velocity. In order to estimate the locations more accurately, we apply a waveform cross-correlation approach to obtain more precise Rayleigh wave arrival times for each station, and then search for the best fitting location using a much finer grid at 0.5° spacing and a model of lateral variations in Rayleigh wave group velocity. We relocate the events in two different ways: (1) single event location, in which we locate each event separately using the Rayleigh wave arrival times at the different stations recording the event and (2) relative event location for events within each cluster, in which we use differential arrival times among the different events recorded at the same station. We only perform relocation for the 14 grade B events because of the very low signal-to-noise of the three grade C events.

3.1. Absolute Location for Single Events

[11] To locate single events, we cross correlate the envelope functions derived from the STA/LTA filter to obtain relative arrival times at each of the stations that recorded an event. By using the envelope functions, we do not need to correct for phase or polarity differences from the source and we also find that the effect of dispersion is small in our band-pass-filtered data. We develop an iterative method to cross correlate the envelope functions with a stack for each event (this stack is the sum of the aligned individual envelopes at each iteration). We use a 20 min window and permit time shifts of ±3.33 min with respect to a reference time defined by the assumed group velocity of 3.955 km/s. The final arrival times are obtained from the shifted traces with a precision of 10 s, and we use only times for which the correlation coefficient between the station envelope functions and the reference stack is 0.5 or greater. Figure 2 shows an example of aligned envelope functions from cross correlation.

[12] We then use these times to search for the best fitting location using a 0.5° × 0.5° grid of points for the Antarctic region. We do not attempt to solve for source depth as we do not have any depth resolution. For each grid point, we follow four steps: (1) Calculate the predicted arrival time at each station based on a Rayleigh wave group velocity map at 50 s obtained from Guy Masters (personal communication, 2010). (2) Find the differences between the observed and predicted times, $dt^i = T^i - T^i_\Delta$. (3) Find the median of these differences, which we treat as the offset to the origin time, $dT_0 = \text{median}(dt)$. (4) Use the L1 norm to find the location that minimizes the absolute value of the residuals, $r^i = dt^i - dT_0$.

[13] The L1 norm for a vector $\mathbf{x}$ is $|\mathbf{x}| = \sum |x_i|$, and the L2 norm is $|\mathbf{x}| = \sqrt{\sum |x_i^2|}$. The L1 norm will reduce the effect of outliers compared with the L2 norm, so it is more robust for low signal-to-noise data. To estimate the statistical uncertainty in our locations we apply a bootstrap approach, in which we randomly resample the available stations and apply our method to get a new location. Repeating this 100 times
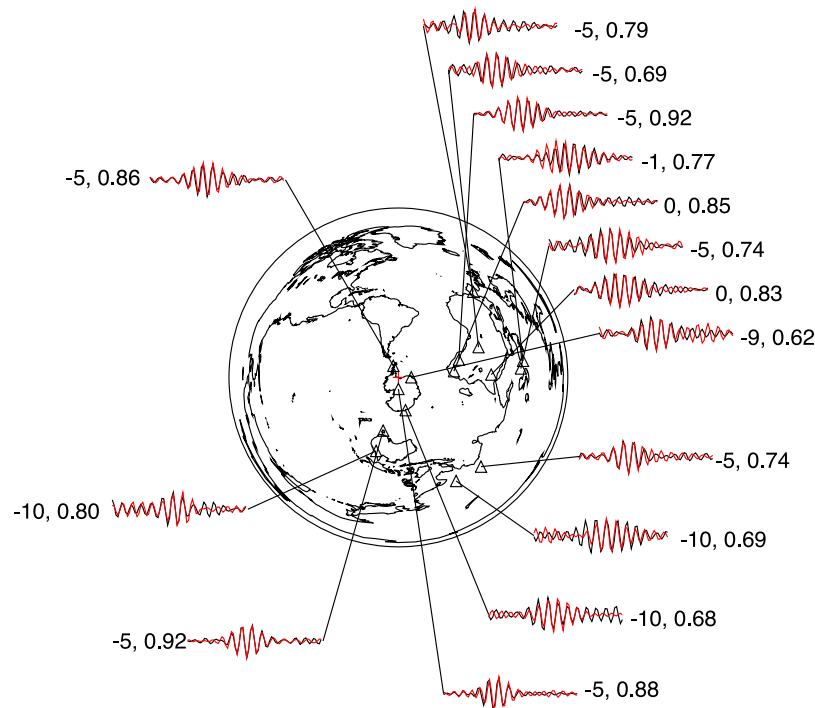
Figure 3. Waveform comparison between two events on the Ronne Ice Shelf. Each time series is 700 s (70 samples) long. The black line is for an event on 2 June 1999; the red line is for an event on 27 June 1999. The first number shows the time shifts in samples (10 s per sample) necessary to align the traces; the second number is the correlation coefficient between the two traces.

provides 100 different location estimates, which we use to compute an approximate confidence ellipsoid.

3.2. Relative Locations for Each Cluster

[14] Our method relies on the fact that closely located events will generate similar waveforms at each station. In this case, we can preserve the polarity and phase information and cross correlate the band-pass-filtered waveforms themselves rather than their envelope functions. For each group, we relatively relocate events using the following procedure:

[15] 1. For each pair of events, cross correlate the waveforms at each station using a 20 min window to get relative arrival times for each pair of events at a resampled time interval of 0.1 s. Figure 3 shows an example of the alignment of seismograms that can be achieved.

[16] 2. Use the individual event locations as starting locations.

[17] 3. Keeping the other event locations fixed at their current locations, search for the best new location for each event using a grid search method that minimizes the L1 norm misfit of the predicted and observed differential times with respect to the other events.

[18] 4. Update all the locations, keeping the centroid of the cluster fixed.

[19] 5. Iterate on steps 3 and 4 until a stable set of locations is obtained.

[20] We use only waveform pairs with correlation coefficients of 0.5 or higher in the location procedure. Using this method, we obtain relative locations for our 13 events, within the three clusters. Both the absolute locations and relative

locations are listed in Table 1. We estimate the errors in relative location to be about 1 degree, much less than the absolute location error ellipses plotted in Figure 6. For the Vanderford Glacier cluster, there is considerable nearby seismicity in 2007 and 2008 listed in the PDE catalog, with two events with magnitudes larger than 5, and there are two other cataloged events in 1984. Because these events are located using body wave arrivals, their absolute location accuracy is likely better than what we can achieve using low signal-to-noise surface waves. Thus, we use a catalog event (M 5.7 on 4 November 2007), as a reference to relocate events within this cluster, and find that three of our events have surface waves that are correlated with this event at several stations. Of these three, the 2005 event lies within the zone of catalog seismicity, the 2001 event locates on the coast to the east of the cataloged events, and the 2002 event lies offshore, however, they are within our location error estimates. The estimated locations for these events are listed in Table 2.

4. Source Mechanisms

[21] Centroid single force (CSF) [*Kanamori and Given*, 1982; *Kawakatsu*, 1989] modeling for uncataloged seismic events in Greenland has indicated horizontal force directions parallel to local ice flow directions [*Tsai and Ekström*, 2007]. These results suggest that such events are associated with horizontal ice mass movement along the expected ice flow directions. Although the CSF model achieved a higher variance reduction than standard centroid moment tensor (CMT) [*Dziewonski et al.*, 1981] solutions, it should be noted that

Table 1. Locations and CSF Solutions for All Events[a]

Area Name	Index	Time	Absolute Location	Relative Location	CSF $(\phi_f(\sigma), \epsilon(\sigma))$	Ms
Ronne Ice Shelf	1	06/02/1999, 17:41:0.0	-78.4°, 310.4°	-78.1°, 310.5°	119° (2°), 0. (0.2)	4.53
	2	06/27/1999, 15:39:20.0	-77.5°, 311.1°	-77.7°, 310.2°	121° (3°), 0.25 (0.15)	4.56
	3	08/04/1999, 8:20:50.0	-77.2°, 311.3°	-77.3°, 310.3°	138° (0.8°), 0. (0.2)	4.36
	4	08/04/1999, 20:54:50.0	-77.4°, 308.6°	-77.4°, 310.4°	112° (25°), 0. (0.1)	4.33
Vanderford Glacier	1	08/09/1997, 12:0:30.0	-67.3°, 109.0°	-66.8°, 109.5°	159° (2.5°), 0. (0.3)	4.28
	2	08/30/2001, 3:47:50.0	-66.1°, 108.9°	-66.5°, 110.4°	154° (1.8°), 0. (0.2)	4.51
	3	05/25/2002, 1:58:20.0	-66.6°, 112.6°	-66.7°, 110.1°	153° (4°), 0. (0.15)	4.34
	4	01/31/2004, 4:33:0.0	-66.4°, 110.5°	-66.8°, 110.3°	142° (8°), 0.35 (0.3)	4.24
	5	11/13/2005, 0:17:50.0	-67.4°, 109.5°	-67.0°, 110.2°	159° (5°), 0. (0.1)	4.39
Ninnis Glacier	1	04/04/1997, 12:20:30.0	-68.4°, 150.5°	-68.3°, 152.3°	35° (2°), 0 (0.3)	4.22
	2	03/14/1998, 10:35:30.0	-68.0°, 150.2°	-68.4°, 151.5°	10° (3°), 0 (0.13)	4.54
	3	01/24/2004, 8:40:30.0	-68.1°, 152.9°	-68.2°, 150.0°	24° (10°), 0. (0.15)	4.37
	4	11/02/2007, 10:2:50.0	-68.7°, 149.8°	-68.3°, 149.6°	30° (3°), 0.2 (0.1)	4.52
	5	06/18/2008, 0:5:30.0	-68.6°, 157.9°	N/A	87° (12°), 0. (0.3)	4.55
Grade C events	C1	03/02/2005, 21:28:0	-67.2°, 136.5°	N/A	N/A	N/A
	C2	05/25/2005, 14:10:40	-72.5°, 142.6°	N/A	N/A	N/A
	C3	05/14/2007, 13:46:30	-72.5°, 155.5°	N/A	N/A	N/A

[a]Locations are in the format of (latitude, longitude).

the single force model cannot always be distinguished seismically from shallow dipping dip-slip faulting earthquakes [e.g., *Dahlen*, 1993]. When the source depth approaches zero for a dip-slip fault, the dominant components in a double-couple solution are M_{xz} and M_{yz} ($\vec{x}$: north, $\vec{y}$: east, $\vec{z}$: vertical), which are usually poorly constrained in practice; thus a modified moment tensor solution using surface point forces is preferred [*Dahlen*, 1993]. The observed Rayleigh wave amplitude measured at 50 s exhibits a two-lobed radiation pattern, and the Love wave, although it typically has a lower signal-to-noise ratio than the Rayleigh wave, has predicted amplitudes comparable in size to the Rayleigh wave. These properties closely match the seismic radiation observed from the Mt. St. Helens landslide, which was analyzed with amplitudes measured at different frequencies in fitting a CSF model [*Kanamori and Given*, 1982]. The surface wave signal for the new events is seen only between about 35 and 70 s period. The lack of observations at longer periods results in an unstable full waveform inversion; therefore, we will solve only for the best fitting single-force horizontal directions for a shallow source that can explain our observed Love and Rayleigh wave amplitudes at 50 s.

[22] To perform our analysis, we first obtain horizontal component seismograms for the events (which were detected using only vertical component data) and rotate them to obtain the transverse and radial components. Next we Fourier transform the Love waves on the transverse component and the Rayleigh waves on both the vertical and radial components to obtain an amplitude spectrum. Then we select waveforms based on their signal-to-noise ratios to perform the inversion. We correct the amplitudes for attenuation and geometrical spreading using *Kanamori and Given* [1981]

$$A(\omega, \phi) = A_{\Delta} e^{\omega a \phi / 2QU} \sqrt{\sin \theta} \qquad (1)$$

where A_{Δ} is the amplitude at each station before correction, a is the Earth radius, ϕ is azimuth, θ is the angular distance between source and station, Q is the effective inverse attenuation along the path, and U is the group velocity. We obtain Q and U estimates from the PREM model [*Dziewonski and Anderson*, 1981] at 50 s period for Love and Rayleigh

waves. Numerical experiments showed that slight changes in Q and U do not affect the overall radiation pattern after the attenuation correction; therefore, we use the same value for all stations. For Love waves, Q is 120, U is 4.36 km/s; for Rayleigh waves, Q is 150, U is 3.887 km/s (the reference velocity in our group velocity map). Surface wave amplitudes at 50 s period are affected both by focusing and defocusing caused by lateral velocity variations and by attenuation heterogeneity. We correct for both effects by computing an amplification factor using a global phase velocity and Q map for Rayleigh [*Dalton and Ekström*, 2006] and Love waves at 50 s period (C. Dalton, personal communication, 2010).

[23] From *Kanamori and Given* [1982], we calculate predicted amplitudes for the Love and Rayleigh waves using

$$A_L = P_L \omega f_0 \hat{s}(\omega) \cos \alpha \sin(\phi_f - \phi_s) \qquad (2a)$$

$$A_R = P_R \omega f_0 \hat{s}(\omega) \cos \alpha \sqrt{\epsilon^2 + \cos(\phi_f - \phi_s)^2} \qquad (2b)$$

where $f_0 \hat{s}(\omega)$ is the source term, ϕ_f and ϕ_s are the azimuths of the horizontal projection of the force direction and the station, α is the angle of the force from horizontal, P_L and P_R are the excitation functions of the Love and Rayleigh waves (which can be obtained from normal mode theory), ϵ describes the relationship between the vertical and horizontal force components, which we treat as a variable from 0 to 1. $f_0 \hat{s}(\omega)$ and α scale the amplitudes and cannot be resolved separately; we only solve for ϕ_f and ϵ. We normalize the observed and predicted amplitudes of the vertical and transverse components, and then search for the combination of ϕ_f and ϵ that minimizes their difference using the L1 norm.

Table 2. Locations Relative to Mw 5.7 Event on 11/04/2007 at (−67.27°, 111.53°)

Time	Location (latitude, longitude)
08/30/2001, 3:47:50.0	-66.90°, 108.95°
11/13/2005, 0:17:50.0	-67.00°, 111.50°
05/25/2002, 1:58:20.0	-65.25°, 107.00°

We do not attempt to solve for the absolute amplitude of the source (which trades off with α), only the orientation of the point force that best fits our observed azimuthal amplitude variations. Because we use only amplitude information (disregarding the phase of the signals), ϕ_f can only be determined modulo 180°, so our results have two possible directions: ϕ_f and ϕ_f +180°. Results are listed in Table 1 and Figure 4 shows a comparison between predicted and observed Rayleigh and Love wave amplitudes as a function of station azimuth. We obtain solutions for the 14 grade B events. To estimate the uncertainty of these solutions, we apply a bootstrap approach similar to that used in the location uncertainty estimation, in which we resample available stations to get a new solution, repeat 100 times, and then estimate the uncertainty from the resulting 100 solutions. The bootstrap results constrain the range of the inferred force directions to within about 15° as given in Table 1. We generally obtain similar force directions among the different events in the three regions, with the exception of an event in 2008 near Ninnis Glacier, which is also in a somewhat different location than other events in the same region.

[24] Although the Rayleigh and Love wave amplitudes observed at individual stations exhibit considerable scatter, the overall amplitude patterns are well captured by our inversion as seen in Figure 4. To test our approach, we also computed synthetic seismograms using an assumed near horizontal thrust fault, which is equivalent to a single horizontal force model in that they generate the same slip vector for the hanging wall (the sliding mass in CSF model) [Dahlen, 1993]. Thus when the vertical slip component is nearly zero, we can link the resolved force direction ϕ (slip vector $\vec{d}(x, y) = (\cos \phi, \sin \phi)$) with rake λ (assumed equal to 90° for a thrust fault) and strike ϕ_f in a CMT solution:

$$\vec{d}(x,y) = \begin{cases} \cos \lambda \cos \phi_f + \sin \lambda \sin \phi_f \\ -\cos \lambda \sin \phi_f + \sin \lambda \cos \phi_f \end{cases} \quad (3)$$

[25] We then compute synthetic waveforms by converting the force direction to strike for a near-horizontal thrust fault with a time constant of 50 s, and using a Green's function calculated from 0.010 to 0.030 Hz and filtered from 0.014 to 0.028 Hz. An example comparison for an event on 27 June 1999 is shown in Figure 5, and the synthetic waveforms agree well with the observed waveforms. Map view of event locations and horizontal force directions are shown in Figure 6.

5. Glacier Dynamic Sources

[26] Over 100 uncataloged seismic events located near the coastline in Greenland were detected with global surface waves [Ekström et al., 2003, 2006]. Those seismic events are linked to calving events at glacier termini given their spatial and temporal correlations from seismic, satellite and GPS observations [Amundson et al., 2008; Joughin et al., 2008; Nettles et al., 2008]. It should be noted that episodes of rapid glacier sliding provide an alternative explanation for the seismic radiation and observed CSF mechanisms. However, an absence of the expected glacier motion during

the seismic events in Greenland argues against this mechanism [Amundson et al., 2008; Nettles et al., 2008], therefore, a calving mechanism is preferred. In Antarctica, teleseismically recorded tidally modulated stick-slip events near the grounding line of the Whillans Ice Stream have been associated with glacier motion recorded by GPS [Wiens et al., 2008]. However, the distinct nucleation and stopping phases noted by Wiens et al. [2008] are not observed in our seismic waveforms. Both our study and the earlier catalog of Ekström [2006] identify a small number of new events near the Antarctic coastline and near glacier termini at some locations [Nettles and Ekström, 2010]. This suggests that these events may originate from similar processes as the Greenland events.

[27] The Greenland events have the following characteristics: (1) locations are near fast-flowing outlet glaciers; (2) waveforms are best fitted with the CSF model, indicating horizontal point forces; (3) inferred force directions are parallel to glacier flow [Tsai and Ekström, 2007]; (4) seasonal variations are correlated with local ice flow rate and calving variations [Joughin et al., 2008; Nettles et al., 2008; Nettles and Ekström, 2010]. However, some of these properties cannot be clearly established for our 17 Antarctic events. Due to the limited detections over 12 years, seasonal variations are not clear, with an almost equal number of events in winter and summer, and the relatively larger location uncertainties prevent a definitive association with glacier termini. For events on Ronne Ice Shelf, the inferred force directions are nearly parallel to the coast and at large angles to the local ice flow vectors. This is untypical for glacial earthquakes, whose single force directions are generally flow-parallel [e.g., Tsai and Ekström, 2007]. We nevertheless suggest glaciological sources for these Antarctic events, because they locate near calving fronts and fast-flowing outlet glaciers (including regions of active rifting) and they are generally separated from regions of cataloged seismicity.

[28] In order to further explore possible connections between glacier calving and our Antarctic events, we analyze images taken with the moderate resolution imaging spectroradiometer (MODIS) onboard NASA's Aqua and Terra satellites. On 250 m resolution images, we compare the Antarctic coastline in the regions of interest before and after our seismic events, confining ourselves to the 14 grade B events. As no MODIS images are available before 2002, and darkness prevents imaging during the winter, we limit the image analysis to two events in the Vanderford Glacier region and two events in the Ninnis Glacier region.

[29] In order to identify possible calving events as glacial earthquake sources, we manually digitize and then compare the coastline before and after the target events. For the four analyzed Antarctic events, the availability of cloud-free MODIS images substantially limits the temporal resolution with which we can identify calving events. We therefore use the following procedure: First, we use the closest available cloud-free image of the entire region of interest including all local fast-moving outlet glaciers within several hundred kilometers of coastline. For three of the four investigated seismic events, we identify coastline changes that may represent calving events. We then focus on these candidate locations using images taken as close to the seismic event origin times as possible. Land fast sea ice can complicate
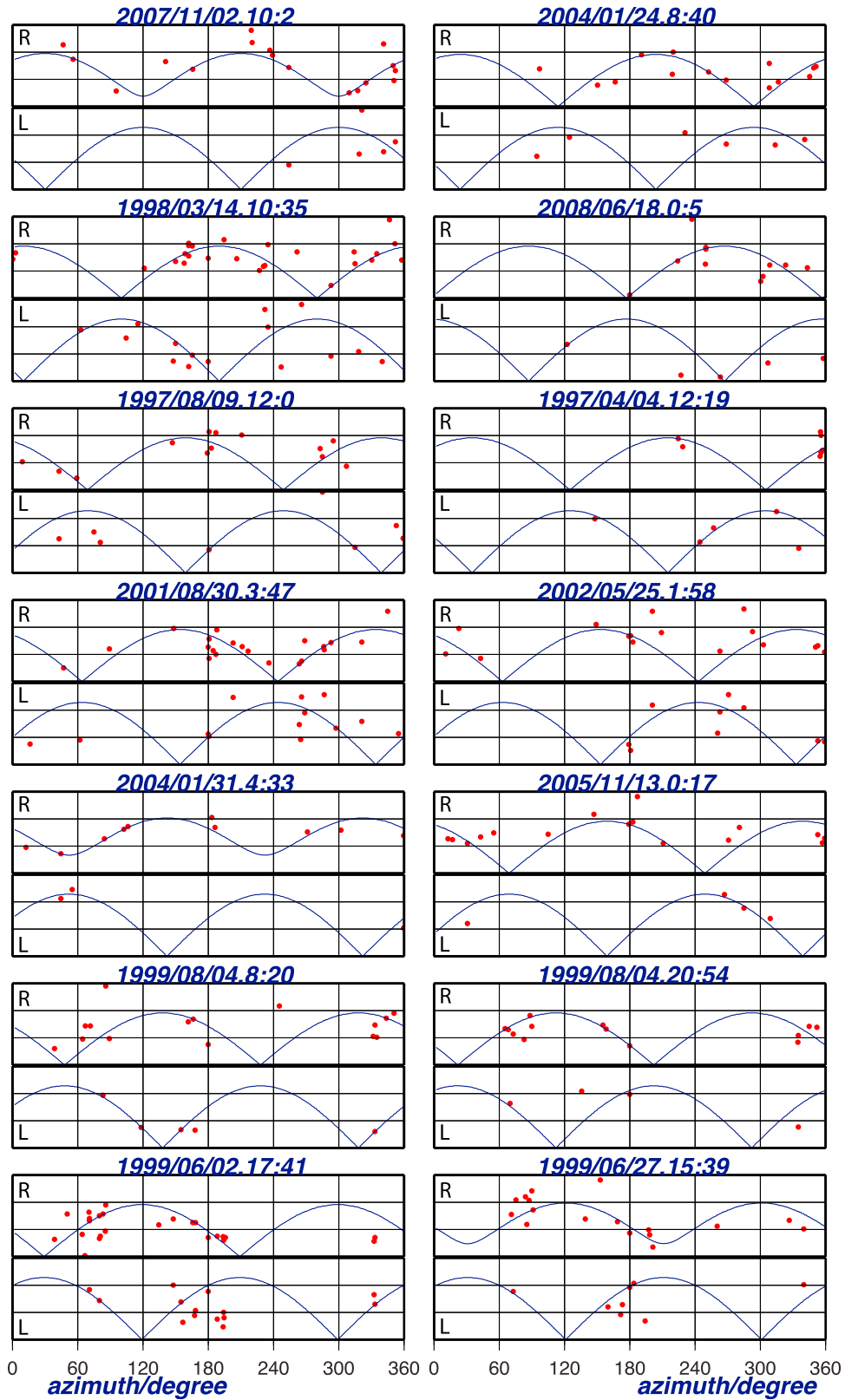
Figure 4. Observed versus predicted amplitudes from a centroid single force (CSF) model. Red dots are observed amplitudes; blue lines are predicted amplitudes using our method. Only relative amplitudes are plotted. "R" indicates Rayleigh wave, "L" indicates Love wave.
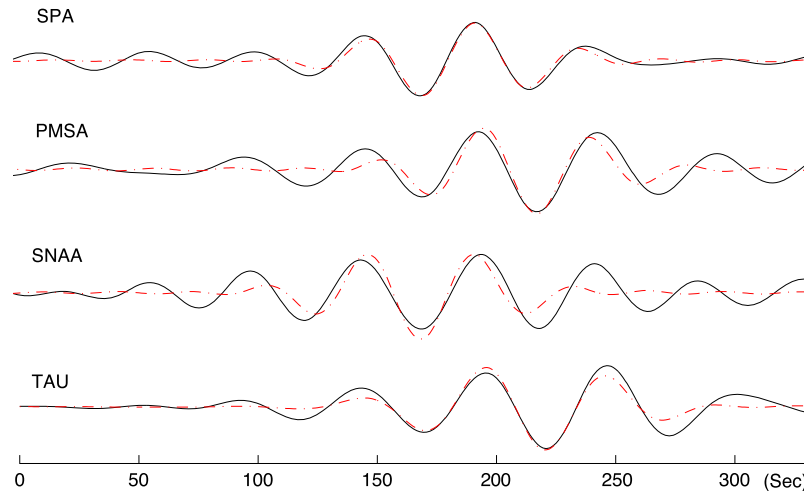
Figure 5. Synthetic waveforms (dashed line) versus recorded waveforms (solid line) at four stations on the "VHZ" channel for a 27 June 1999, event on the Ronne Ice Shelf. Waveforms are filtered between 0.014 Hz and 0.028 Hz. Synthetic waveforms are generated with an equivalent double-couple source instead of CSF source.

interpretations, because it is often difficult to distinguish from land-sourced ice. In addition, owing to its coarse temporal resolution, our procedure can miss calving events, because ice flow may fill in the missing ice before a cloud-free, postcalving image becomes available. Nevertheless, our analysis does identify possible individual calving events as candidates for causing the seismic events and thus provides potential constraints on their source mechanisms.
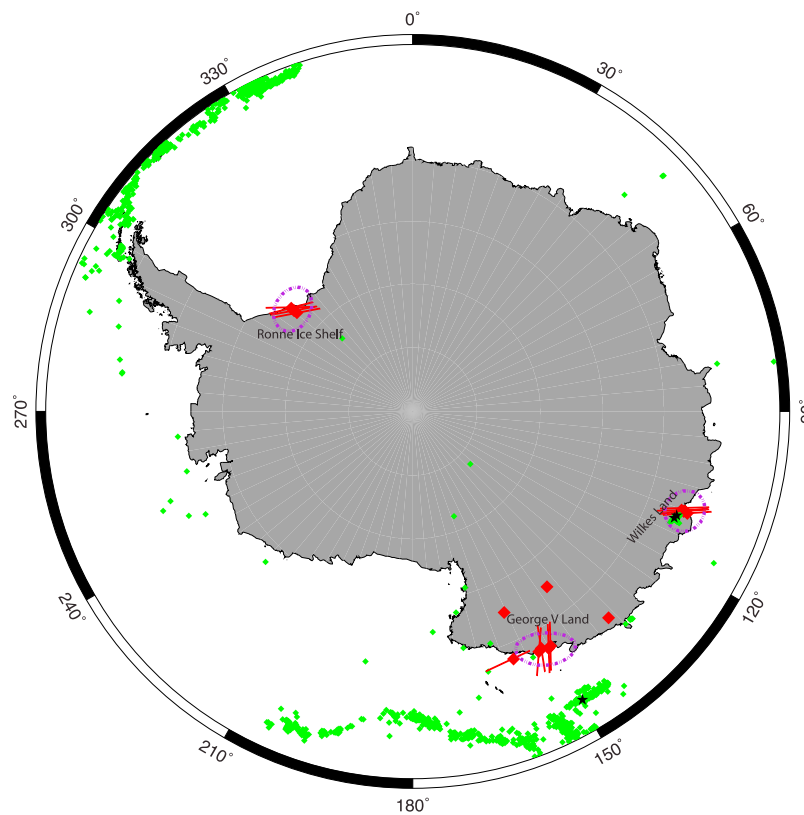
Figure 6. Antarctic map with our new events (red) and existing catalog events (green). Black stars are catalog events greater than M 5. The red lines are our computed force directions. Purple circles are 95% absolute location uncertainties.
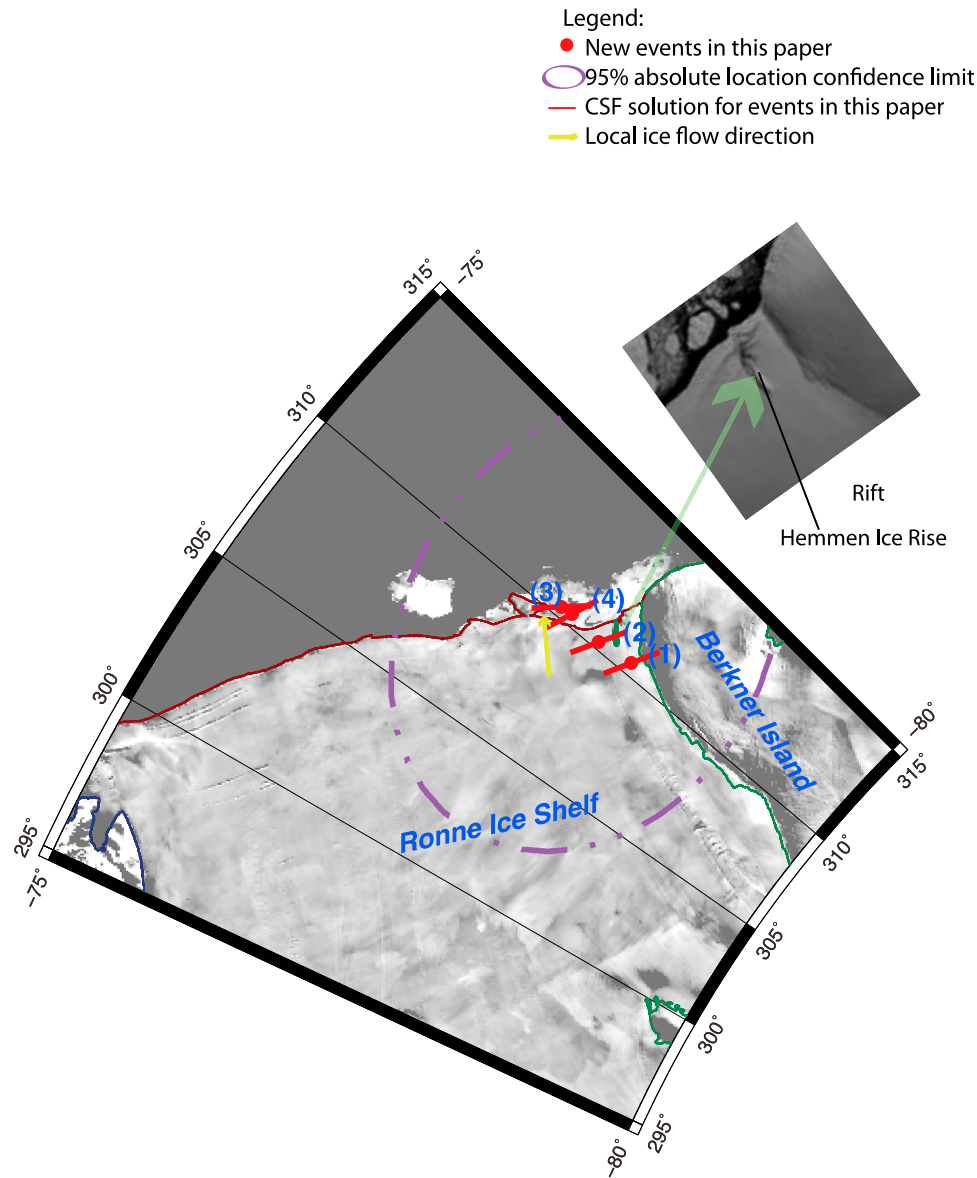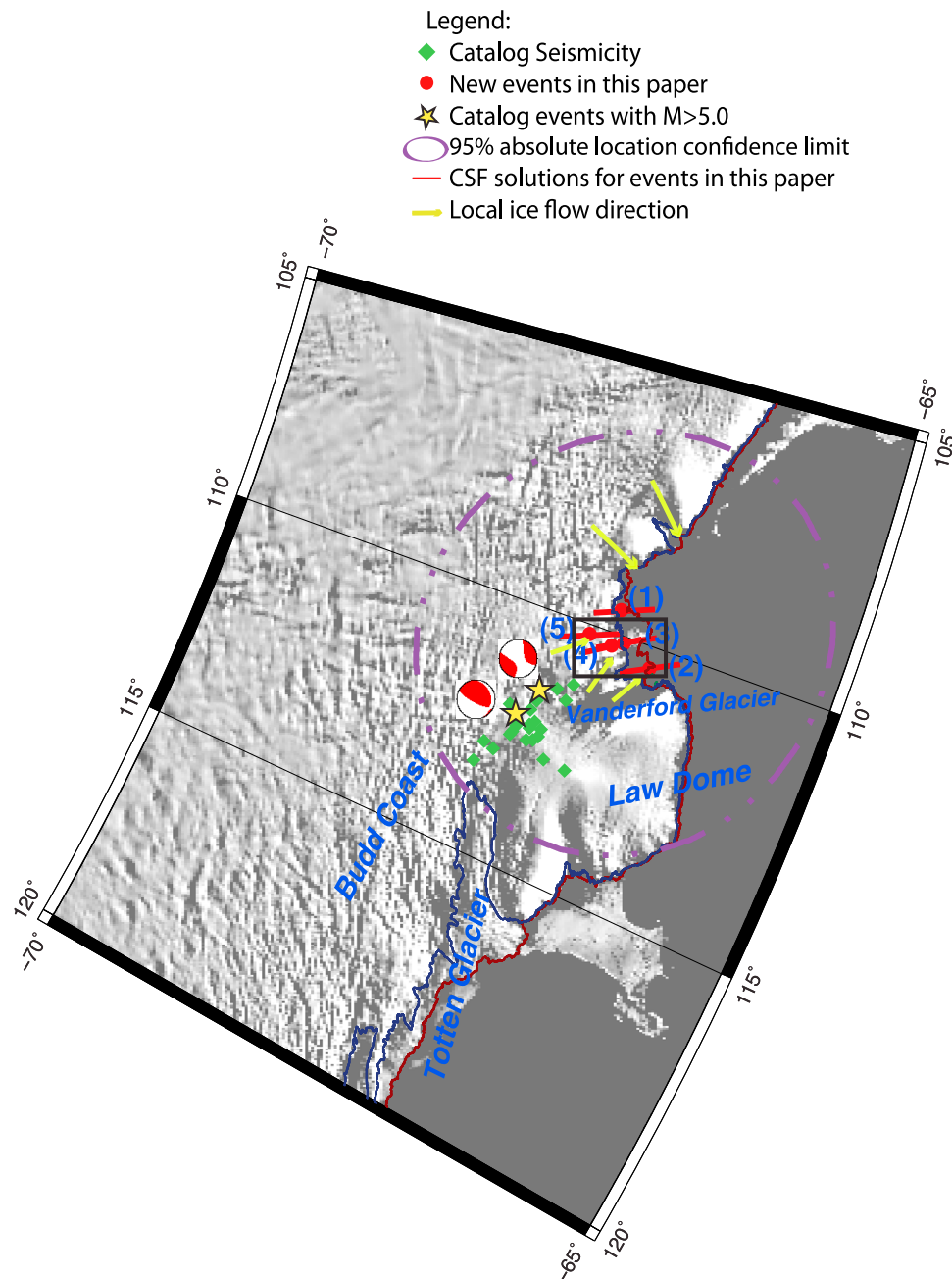
Figure 7. Map for events in the Ronne Ice Shelf. The background is the MOA image with 60% transparency, solid grey is ocean. The red line is the ice front, the green line delimits islands and ice rises. A close-up of a rift and the Hemmen Ice Rise are shown in the MOA satellite image. Index numbers of events in each region correspond to events in Table 1. Coastline and grounding lines are from *Scambos et al.* [2007].

5.1. Ronne Ice Shelf

[30] Four of our events (all grade B) are clustered toward the front of the Ronne Ice Shelf, near Hemmen Ice Rise (HIR) west of Berkner Island (BI) (Figure 7). All four events occurred in either June or August 1999 and their waveforms are well correlated, indicating that they have similar source mechanisms. Their force directions are consistent, and are mostly well constrained as indicated by the bootstrap test. The event occurring at 20:00 on 4 August 1999 shows ambiguity in the force direction with two separate peaks in the bootstrap result, but synthetic waveforms show a better fit with the force direction at about 120°, consistent with the other three events. This region was the site of a large calving event in October 1998 (which produced icebergs A-38 and A-39)

[*Lazzara et al.*, 2008], however, the calving itself is not detected with our method probably due to the large tabular iceberg involved in the calving event instead of a capsizing iceberg. There are no high-resolution MODIS images available for this region during this time period. In contrast to the documented Greenland glacial earthquakes [e.g., *Nettles and Ekström*, 2010], the force directions are perpendicular to the background ice shelf velocity vector. This argues against a typical calving generating mechanism. Instead, the force direction is parallel to the rift propagation direction [see *Rignot and MacAyeal*, 1998, Figure 2]. Rift-related icequakes have been observed to concentrate at the rift tip as well as distribute along the rift, but at magnitudes lower than 3 [*Bassis et al.*, 2007; *Winberry and Anandakrishnan*, 2003]. It is possible that our detected events are associated

Figure 8. Map for events near Vanderford Glacier. The background is the MOA image with 60% transparency, solid grey is ocean. The blue line is the glacier grounding line; the red line is the ice front. Index numbers of events in each region correspond to events in Table 1. Coastline and grounding lines are from *Scambos et al.* [2007]. The black box indicates the approximate locations of MODIS images in Figure 9 and 10. Moment tensor solutions for two M > 5 catalog events are from the Global CMT project.

with the development of a new rift system after the calving event in 1998. The spatiotemporal distribution of the relocated events may relate to the development of different rifts in this region [*Larour et al.*, 2004]. However, the physics of how rift-related ice movements could generate observable long-period seismic energy is not clear.

5.2. Vanderford Glacier

[31] Five of our events (all grade B) cluster near the calving front of Vanderford Glacier in Wilkes Land. Vanderford

Glacier is located in a deep subglacial trench and is bounded to its north by Law Dome (Figure 8). *Pritchard et al.* [2009] showed that this glacier is currently undergoing dynamic thinning [*Pritchard et al.*, 2009, Figure S8]. There has recently been high cataloged seismicity near 67° S, 110° E, in 2007 and 2008: about twenty events occurred during those two years, compared to only two events recorded before 2007. Two M ≥ 5 earthquakes occurred in November 2007 and July 2008, and there were also two magnitude 5 cataloged earthquakes on 19 May 1984. These events locate in the
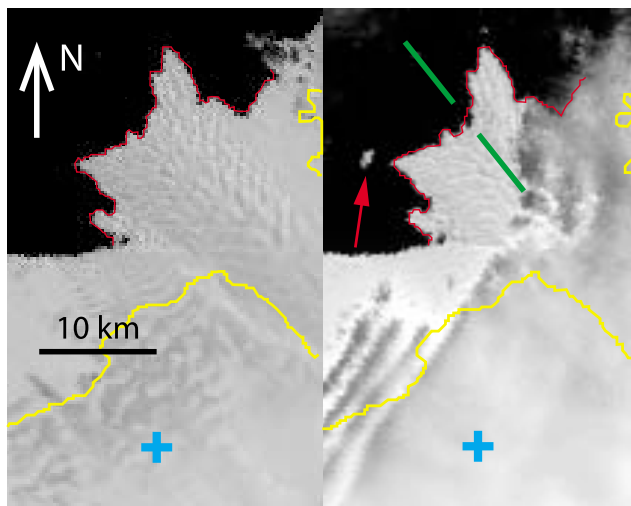
Figure 9. MODIS images depicting a calving event as a possible source for event 4 in the Vanderford region (Table 1). The images were taken on 21 January and 5 February 2004, 10 days before and 5 days after the event origin time, respectively. The red line traces the precalving ice front, whereas the yellow line marks the ice sheet grounding line [*Scambos et al.*, 2007]. The cyan cross indicates the nominal seismic event location (the entire image is within the location error ellipse) and the green lines show the estimated horizontal force directions (±180°). The red arrow points to an iceberg, which likely detached during the calving event.

valley that connects Vanderford Glacier and separates the Law Dome ice cap from the East Antarctic ice sheet, farther inland than the coastal regions where our new events are located. The CMT solutions for larger events exhibit considerable variations and include a substantial non double-couple component for the 1984 event. Only the July 2008 event has a shallow thrust faulting mechanism, matching the mechanism for a possible landslide event. However, the fault orientation is not consistent with the ice flow directions. Therefore, it is likely that these cataloged events are of tectonic origin and are unrelated to our Antarctic events. The new events locate along the East Antarctic coastline, and their force directions are consistent with local ice flow directions (I. Joughin, personal communication, 2009) at different locations. The agreement indicates these events may relate to ice dynamic processes, such as calving, basal sliding or stick-slip motion similar to those that have been observed from West Antarctica's ice streams [*Wiens et al.*, 2008].

[32] For events 4 and 5 of the Vanderford region (Table 1), we identified calving events on the MODIS images as possible seismic sources. Figure 9 shows a pair of images taken 10 days before and 5 days after event 4. The images clearly show evidence of a calving event that occurred between the images. The calving area amounts to about 1.5 km^2, approximately corresponding to the size of a nearby iceberg (red arrow). Figure 10 illustrates another calving event on the Vanderford ice front. The three images were taken 1 day before, 7 min after, and 8 days after the origin time of event 5. Little change is apparent between the first and second image. However, assuming that a major calving event coincided with event 5, we expect ice debris to occupy the calved terminus

portion immediately after the event. Thus, as the second image was taken within a few minutes of our event origin time, it is unlikely to exhibit any changes at our 250 m resolution. On the other hand, the third image, taken about a week after the event, does show evidence for a calving event with an area of about 2 km^2. The locations and expected horizontal force directions are within our estimated source uncertainties, which further supports the association between the seismic events and calving episodes. The sizes of icebergs involved in the calving events are comparable to the size of icebergs involved in glacial earthquakes observed in Greenland [*Amundson et al.*, 2008]. Considering the proximity of other events in this region, it is likely that they originate from the same mechanism as events 4 and 5, however, the lack of MODIS images prevents additional investigation.
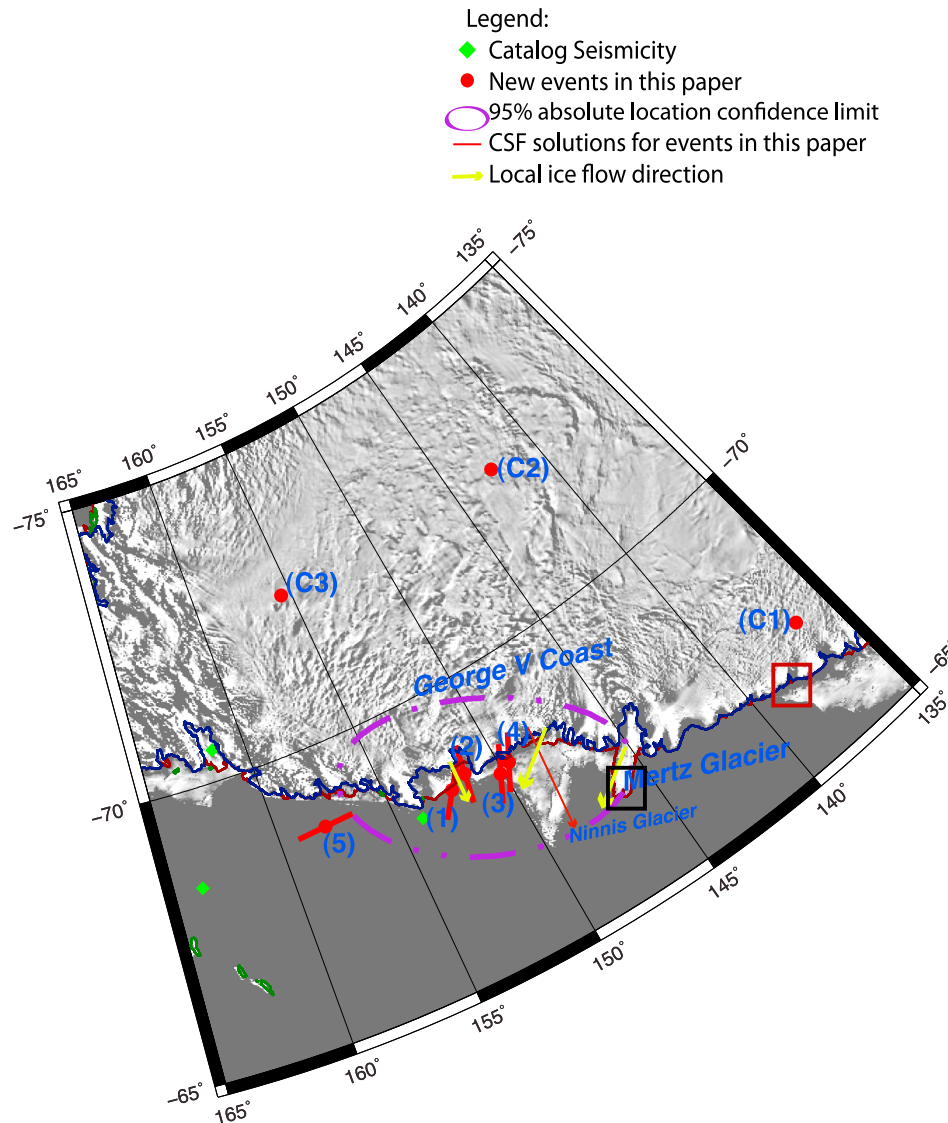
5.3. Ninnis Glacier

[33] Eight of our events (five grade B events and three grade C events) locate on George V Coast, of which four grade B events cluster between Ninnis Glacier and Cook Iceshelf, while one event lies to their west and offshore (Figure 11). The waveforms of the grade C events have lower signal-to-noise ratios, preventing the more detailed analyses we performed for the grade B events. Therefore, we do not have CSF solutions and refined locations for these three events. Four of the grade B events near Ninnis Glacier show force directions consistent with the local ice flow directions (I. Joughin, personal communication, 2009), while the event to their west has a force direction nearly parallel to the coastline. The agreement between local ice flow directions
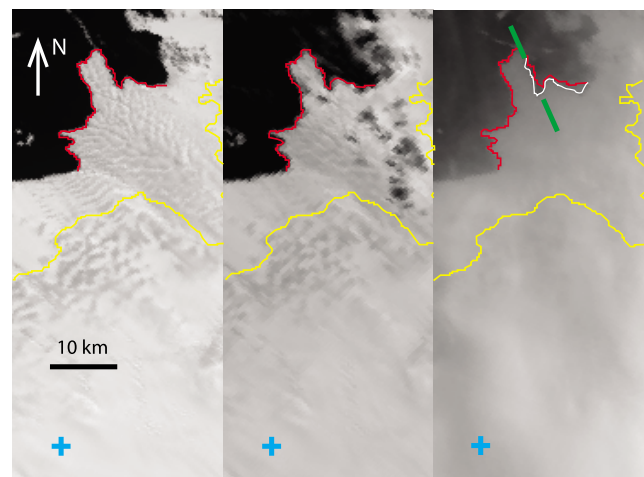
Figure 10. MODIS images depicting a calving event as a possible source for event 5 in the Vanderford region (Table 1). The images were taken on 12 November, 13 November, and 21 November 2005. This corresponds to 1 day before, 7 min after, and 8 days after the event origin time. The red line traces the precalving ice front, whereas the yellow line marks the ice sheet grounding line [*Scambos et al.*, 2007]. Due to poor lightening, a white line is added to the rightmost image tracing the after calving ice front, to better highlight the calving event. The cyan cross indicates the nominal seismic event location (the entire image is within the location error ellipse) and the green lines show the estimated horizontal force directions (±180°).

Figure 11. Map for events near Ninnis Glacier. The background is the MOA image with 60% transparency, solid grey is ocean. The blue line is the glacier grounding line; the red line is the ice front. Index numbers of events in each region correspond to events in Table 1. Coastline and grounding lines are from *Scambos et al.* [2007]. The red box indicates the approximate location of MODIS images in Figure 12. The black box indicates the approximate location of images in Figure 13.

and computed force directions strongly suggests that those events are related to glaciological processes. This region has complex bathymetry, with floating Ninnis and Mertz glacier tongues close to Ninnis Bank and Mertz Bank and numerous small grounded icebergs and deformed stationary sea ice [*Massom*, 2003]. There was one major calving event from Ninnis Glacier in 2000 and a calving event from Mertz Glacier in 2010. The calving event in 2000 was from the floating Ninnis glacier tongue, and the complete development of the crack is a slow but gradual process, which took 10 years to complete [*Massom*, 2003], and likely did not generate any discrete events fast and energetic enough to be seen with our surface wave detector.

[34] The offshore seismic event with a force direction parallel to the coast line is aligned with the westward ocean currents within the East Wind Drift zone [*Massom*, 2003].
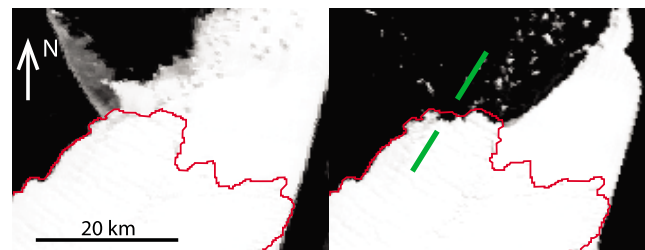
Figure 12. MODIS images depicting a calving event as a possible source for event 4 in the Ninnis region (Table 1). The images were taken on 27 October and 8 November 2004, 6 days before and 6 days after the event origin time, respectively. The red line traces the precalving ice front. The epicentral location is about 250 km to the southeast. The green lines show the estimated horizontal force directions (±180°).
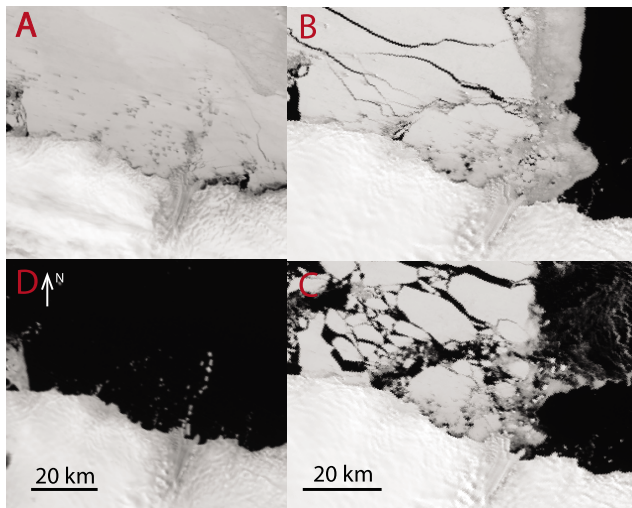
Figure 13. MODIS images of a changing glacier tongue in the Ninnis region. The images were taken on (a) 2 January 2004 (22 days before the calving event), (b) 23 January (1 day before the calving event), (c) 27 January (4 days after the calving event), and (d) 9 February (16 days after the calving event). This ice front locates almost 550 km away from the calculated seismic epicenter making the association between glacial earthquake and depicted ice front changes somewhat speculative.

However, interactions between drifting icebergs and sea ice are not likely to produce a recordable seismic surface wave. One possible explanation for this event is crustal uplift due to postglacial rebound. *James and Ivins* [1998, Figure 13] and *Kreemer and Holt* [2000, Figure 3] show that the expected crustal motion is at a similar direction to this event, suggesting a possible link between them. There was an Mw 8.0 earthquake 500 km off the coast near Balleny Island in March 1998, close to the plate boundary, but the fault plane and moment tensor solution suggest that this was an intraplate earthquake [*Nettles et al.*, 1999]. Some studies suggested that this large earthquake may be caused by postglacial rebound [*Kreemer and Holt*, 2000; *Tsuboi et al.*, 2000], and the fault plane orientation agrees with the modeled crustal response from deglaciation [*Kreemer and Holt*, 2000]. However, detailed strain field analysis is beyond the scope of this paper.

[35] For Ninnis events 3 and 4 (Table 1) MODIS images of the coastline are available. Figure 12 shows an image pair of the Mertz Glacier tongue taken 6 days before and 6 days after the origin time of event 4. The images illustrate the breakup of a large portion of the sea ice attached to the glacier front. Furthermore, the ice tongue loses an area of 2 km^2 or more over this time period. It should be noted that our epicentral location for the corresponding event is almost 250 km to the southeast of the calving event, which is near the upper limit of the location error estimates. Nonetheless, the expected force direction from this calving event is consistent with our estimated force direction, supporting an association with the detected seismic event.

[36] For Ninnis event 3 the images do not reveal calving events as clearly as the previously presented cases. Near the event's epicenter a large intact sea ice cover exists, which complicates identification of coastline changes. However, some cloud-free images reveal potentially relevant ice front changes for a small ice stream approximately 300 km west of the Mertz glacier (Figure 13), almost 550 km away from the calculated seismic epicenter. Whereas this large distance calls into question the role of this calving event in generating the seismic event, we could not identify any ice front changes closer to the epicenter. Figure 13a shows that three weeks before the origin time of event 3 an intact sea ice cover embraces the glacier's front. Within 16 days after the event, the sea ice cover has completely disappeared and several large icebergs have detached from the terminus (Figure 13d). Whereas the sea ice cover inhibits detailed inspection closer to the event origin time, it is clear that significant changes are happening between 1 day before (Figure 13b) and 3 days after (Figure 13c) the event origin time. It is possible that the image changes are caused by iceberg collision or capsizing, which have been suggested as glacial earthquake sources [*Amundson et al.*, 2008; *Tsai et al.*, 2008].

6. Discussion

[37] Our observations suggest a variety of potential generating mechanisms for seismic events in Antarctica. The three calving events revealed by satellite images as well as the agreement between calculated horizontal force directions and ice flow directions suggest an association with the observed seismic events. The termini conditions for Antarctica events are different from previous reported seismic events in Greenland. The three calving events in Antarctica are from floating glacier tongues, while events in Greenland are mostly from grounded termini or near floating termini. A contact with the ocean floor provides force coupling with the solid Earth, and excites seismic energy at the observed periods [*Amundson et al.*, 2008; *Nettles and Ekström*, 2010]. Observations of glacial earthquakes in Antarctica are rare, and there are several known large calving events missing from our list, e.g., two major events in 1998 and 2000 from the Ronne Ice Shelf, two in 2000 from the Ross Ice Shelf [*Lazzara et al.*, 2008], and one in 2000 from Ninnis Glacier [*Massom*, 2003].

[38] One possible reason for the different levels of detection between Greenland and Antarctica events can be attributed to differences in calving styles. Observations and mechanical modeling studies point out that capsizing icebergs interacting with surrounding ice mélange are able to produce effective horizontal forces at a ~50 s timescale [*Tsai et al.*, 2008; *Amundson et al.*, 2010], and are therefore a preferred mechanism. Grounded tidewater glaciers predominantly produce relatively narrow icebergs prone to capsizing and thus are more likely to generate glacial earthquakes. For Jakobshavn Isbræ, in Western Greenland, for example, this style of calving occurs mostly during later spring and summer. In early spring, however, the glacier loses its floating tongue, which temporarily develops during the winter, via the calving of tabular icebergs. As these icebergs have larger horizontal dimensions than vertical, they do not capsize [*Amundson et al.*, 2010]. This latter calving style is "quiet" in that it does not produce substantial amounts of low-frequency seismicity [*Nettles and Ekström*, 2010]. Although calving off grounded termini is typical for temperate tidewater glaciers, the current conditions at Greenland's outlet

glaciers as well as recent observations at Columbia Glacier [*Walter et al.*, 2010] demonstrate that calving styles can spontaneously change. This may be a side effect of glacier thinning, terminus retreat into deeper water [*Walter et al.*, 2010] or changing ocean temperatures [*Holland et al.*, 2008; *Murray et al.*, 2010].

[39] For floating Antarctic ice shelves, calving mass loss occurs mostly via large tabular icebergs [*Lazzara et al.*, 2008], which do not capsize and thus produce little low-frequency energy. Iceberg capsizing does play an important role during occasional ice shelf collapses as observed at the Larsen A and B Ice Shelves [*MacAyeal et al.*, 2003]. However, even such sudden ice shelf disintegration processes cause few or no glacial earthquakes [*Nettles and Ekström*, 2010]. This suggests that in addition to calving style, lack of seismic coupling to the Earth inhibits transmission of low-frequency seismic energy during calving events off floating ice fronts.

[40] The present analysis of global seismograms and satellite images indicates that, although less frequently than in Greenland, Antarctic ice fronts occasionally calve capsizing icebergs, transferring low-frequency seismic energy into the Earth. For the three likely calving events identified from satellite imagery, the narrow and irregular shapes of the icebergs make it possible to produce capsizing icebergs during the calving process. For the Vanderford events, the geometry of the calved portion and its relative proximity to grounding lines (about 20 km, see Figure 9) may enable energy transmission to the solid Earth.

[41] Similar to the mélange in Greenland's fjords, an intact sea ice cover near the calving fronts may play an important role during the generation of low-frequency seismicity. The Mertz glacier calving event pushed away part of the sea ice in front of the glacier tongue. The location of the calving event is close to Mertz Bank, with depths shallower than about 500 m and "trapped" small icebergs [*Massom*, 2003]. The presence of small icebergs and sea ice possibly provide resistant forces similar to ice mélange. Moreover, considering the thickness of Mertz Glacier is approximately 300 to 600 m [*Legrésy et al.*, 2004], the contact of a capsizing iceberg with the ocean floor is highly possible. However, a detailed mechanical force analysis for these calving events will require bathymetry and ice thickness data, as well as images with higher temporal resolution (our current temporal resolution is several days).

7. Conclusions

[42] Our results, as well as those of *Ekström* [2006], show that global surface wave detectors applied to continuous records from the global seismic network are capable of identifying hundreds of new seismic events that are not listed in existing earthquake catalogs. Most of these are tectonic earthquakes that are either too small, or radiate too little body wave energy, to be detected using standard methods. However, there are also many seismic events detected in Greenland, which have been linked to calving events by several different studies [*Amundson et al.*, 2008; *Joughin et al.*, 2008; *Nettles et al.*, 2008], and a small number of seismic events in Antarctica. Due to their poor signal-to-noise and the sparse global station distribution near Antarctica, it is difficult to obtain accurate locations and resolve

source mechanisms for those events. We use waveform correlation and a global Rayleigh wave velocity model at 50 s to relocate these events, and find generally good agreement with glacier termini at Vanderford Glacier and Ninnis Glacier. Bootstrap resampling tests show that the horizontal force directions estimated using a CSF source model are well constrained. Satellite images link three seismic events with apparent calving events that are either close to grounding lines or surrounded by sea ice cover. Based on their locations, force directions, and satellite evidence, we associate events near Vanderford Glacier and Ninnis Glacier with calving events or other ice dynamic processes. However, one exception is the event in 2008 near Ninnis Glacier, which is best explained by postglacial rebound. Events on the Ronne Ice Shelf are not near any fast-flowing glacier termini but are very close to rifts and islands, and are likely best explained by processes related to rift propagation, considering that their force directions are parallel to local rift directions. Detection of additional Antarctic events by local seismic networks would help to draw stronger conclusions, and complementary observation methods such as GPS, InSAR and satellite images with higher temporal resolution would aid in distinguishing between different generating mechanisms.

References

Amundson, J. M., M. Truffer, M. P. Lüthi, M. Fahnestock, M. West, and R. J. Motyka (2008), Glacier, fjord, and seismic response to recent large calving events, Jakobshavn Isbræ, Greenland, *Geophys. Res. Lett.*, *35*, L22501, doi:10.1029/2008GL035281.

Amundson, J. M., M. Fahnestock, M. Truffer, J. Brown, M. P. Lüthi, and R. J. Motyka (2010), Ice mélange dynamics and implications for terminus stability, Jakobshavn Isbræ, Greenland, *J. Geophys. Res.*, *115*, F01005, doi:10.1029/2009JF001405.

Anandakrishnan, S., and R. B. Alley (1997), Stagnation of ice stream C, West Antarctica by water piracy, *Geophys. Res. Lett.*, *24*(3), 265–268.

Bassis, J. N., H. A. Fricker, R. Coleman, Y. Bock, J. Behrens, D. Darnell, M. Okal, and J. B. Minster (2007), Seismicity and deformation associated with ice-shelf rift propagation, *J. Glaciol.*, *53*(183), 523–536.

Dahlen, F. A. (1993), Single-force representation of shallow landslide sources, *Bull. Seismol. Soc. Am.*, *83*(1), 130–143.

Dalton, C. A., and G. Ekström (2006), Global models of surface wave attenuation, *J. Geophys. Res.*, *111*, B05317, doi:10.1029/2005JB003997.

Danesi, S., S. Bannister, and A. Morelli (2007), Repeating earthquakes from rupture of an asperity under an Antarctic outlet glacier, *Earth Planet. Sci. Lett.*, *253*(1–2), 151–158.

de Juan, J., et al. (2010), Sudden increase in tidal response linked to calving and acceleration at a large Greenland outlet glacier, *Geophys. Res. Lett.*, *37*, L12501, doi:10.1029/2010GL043289.

Dziewonski, A. M., and D. L. Anderson (1981), Preliminary reference Earth model, *Phys. Earth Planet. Inter.*, *25*(4), 297–356.

Dziewonski, A. M., T. A. Chou, and J. H. Woodhouse (1981), Determination of earthquake source parameters from waveform data for studies of global and regional seismicity, *J. Geophys. Res.*, *86*, 2825–2852.

Ekström, G. (2006), Global detection and location of seismic sources by using surface waves, *Bull. Seismol. Soc. Am.*, *96*(4A), 1201–1212.

Ekström, G., M. Nettles, and G. A. Abers (2003), Glacial earthquakes, *Science*, *302*(5645), 622–624.

Ekström, G., M. Nettles, and V. C. Tsai (2006), Seasonality and increasing frequency of Greenland glacial earthquakes, *Science*, *311*(5768), 1756–1758.

Holland, P. R., A. Jenkins, and D. M. Holland (2008), The response of ice shelf basal melting to variations in ocean temperature, *J. Clim.*, *21*(11), 2558–2572.

James, T. S., and E. R. Ivins (1995), Present-day Antarctic ice mass changes and crustal motion, *Geophys. Res. Lett.*, *22*(8), 973–976.

James, T. S., and E. R. Ivins (1998), Predictions of Antarctic crustal motions driven by present-day ice sheet evolution and by isostatic memory of the Last Glacial Maximum, *J. Geophys. Res.*, *103*, 4993–5017.

Joughin, I. (2002), Ice-sheet velocity mapping: A combined interferometric and speckle-tracking approach, *Ann. Glaciol.*, *34*, 195–201.

Joughin, I., I. Howat, R. B. Alley, G. Ekström, M. Fahnestock, T. Moon, M. Nettles, M. Truffer, and V. C. Tsai (2008), Ice front variation and tidewater behavior on Helheim and Kangerdlugssuaq glaciers, Greenland, *J. Geophys. Res.*, *113*, F01004, doi:10.1029/2007JF000837.

Kanamori, H., and J. W. Given (1981), Use of long-period surface-waves for rapid-determination of earthquake-source parameters, *Phys. Earth Planet. Inter.*, *27*(1), 8–31.

Kanamori, H., and J. W. Given (1982), Analysis of long-period seismic waves excited by the May 18, 1980, eruption of Mount St. Helens: A terrestrial monopole, *J. Geophys. Res.*, *87*, 5422–5432.

Kawakatsu, H. (1989), Centroid single force inversion of seismic waves generated by landslides, *J. Geophys. Res.*, *94*, 12,363–12,374.

Kreemer, C., and W. E. Holt (2000), What caused the March 25, 1998 Antarctic plate earthquake?: Inferences from regional stress and strain rate fields, *Geophys. Res. Lett.*, *27*(15), 2297–2300.

Larour, E., E. Rignot, and D. Aubry (2004), Modelling of rift propagation on Ronne Ice Shelf, Antarctica, and sensitivity to climate change, *Geophys. Res. Lett.*, *31*, L16404, doi:10.1029/2004GL020077.

Lazzara, M. A., K. C. Jezek, T. A. Scambos, D. R. MacAyeal, and C. J. van der Veen (2008), On the recent calving of icebergs from the Ross Ice Shelf, *Polar Geogr.*, *23*(3), 201–212.

Legrésy, B., A. Wendt, I. Tabacco, F. Rémy, and R. Dietrich (2004), Influence of tides and tidal current on Mertz Glacier, Antarctica, *J. Glaciol.*, *50*, 427–435.

MacAyeal, D. R., T. A. Scambos, C. I. Hulbe, and M. A. Fahnestock (2003), Catastrophic ice-shelf break-up by an ice-shelf-fragment-capsize mechanism, *J. Glaciol.*, *49*, 22–36.

Massom, R. A. (2003), Recent iceberg calving events in the Ninnis Glacier region, East Antarctica, *Antarct. Sci.*, *15*(2), 303–313.

Murray, T., et al. (2010), Ocean regulation hypothesis for glacier dynamics in southeast Greenland and implications for ice sheet mass changes, *J. Geophys. Res.*, *115*, F03026, doi:10.1029/2009JF001522.

Neave, K. G., and J. C. Savage (1970), Icequakes on the Athabasca Glacier, *J. Geophys. Res.*, *75*, 1351–1362.

Nettles, M., and G. Ekström (2010), Glacial earthquakes in Greenland and Antarctica, *Annu. Rev. Earth Planet. Sci.*, *38*, 467–491, doi:10.1146/annurev-earth-040809-152414.

Nettles, M., T. C. Wallace, and S. L. Beck (1999), The March 25, 1998 Antarctic plate earthquake, *Geophys. Res. Lett.*, *26*(14), 2097–2100.

Nettles, M., et al. (2008), Step-wise changes in glacier flow speed coincide with calving and glacial earthquakes at Helheim Glacier, Greenland, *Geophys. Res. Lett.*, *35*, L24503, doi:10.1029/2008GL036127.

O'Neel, S., H. P. Marshall, D. E. McNamara, and W. T. Pfeffer (2007), Seismic detection and analysis of icequakes at Columbia Glacier, Alaska, *J. Geophys. Res.*, *112*, F03S23, doi:10.1029/2006JF000595.

Pritchard, H. D., R. J. Arthern, D. G. Vaughan, and L. A. Edwards (2009), Extensive dynamic thinning on the margins of the Greenland and Antarctic ice sheets, *Nature*, *461*, 971–975, doi:10.1038/nature08471.

Rignot, E., and D. R. MacAyeal (1998), Ice-shelf dynamics near the front of the Filchner-Ronne Ice Shelf, Antarctica, revealed by SAR interferometry, *J. Glaciol.*, *44*, 405–418.

Scambos, T. A., T. M. Haran, M. A. Fahnestock, T. H. Painter, and J. Bohlander (2007), MODIS-based Mosaic of Antarctica (MOA) data sets: Continent-wide surface morphology and snow grain size, *Remote Sens. Environ.*, *111*(2–3), 242–257, doi:10.1016/j.rse.2006.12.020.

Shearer, P. M. (1991), Imaging global body wave phases by stacking long-period seismograms, *J. Geophys. Res.*, *96*, 20,353–20,364.

Shearer, P. M. (1994), Global seismic event detection using a matched-filter on long-period seismograms, *J. Geophys. Res.*, *99*, 13,713–13,725.

Tsai, V. C., and G. Ekström (2007), Analysis of glacial earthquakes, *J. Geophys. Res.*, *112*, F03S22, doi:10.1029/2006JF000596.

Tsai, V. C., J. R. Rice, and M. Fahnestock (2008), Possible mechanisms for glacial earthquakes, *J. Geophys. Res.*, *113*, F03014, doi:10.1029/2007JF000944.

Tsuboi, S., M. Kikuchi, Y. Yamanaka, and M. Kanao (2000), The March 25, 1998 antarctic earthquake: Great earthquake caused by postglacial rebound, *Earth Planets Space*, *52*(2), 133–136.

Walter, F., J. F. Clinton, N. Deichmann, D. S. Dreger, S. E. Minson, and M. Funk (2009), Moment tensor inversions of icequakes on Gornergletscher, Switzerland, *Bull. Seismol. Soc. Am.*, *99*(2A), 852–870.

Walter, F., S. O'Neel, D. McNamara, W. T. Pfeffer, J. N. Bassis, and H. A. Fricker (2010), Iceberg calving during transition from grounded to floating ice: Columbia Glacier, Alaska, *Geophys. Res. Lett.*, *37*, L15501, doi:10.1029/2010GL043201.

Wiens, D. A., S. Anandakrishnan, J. P. Winberry, and M. A. King (2008), Simultaneous teleseismic and geodetic observations of the stick-slip motion of an Antarctic ice stream, *Nature*, *435*, 770–774, doi:10.1038/nature06990.

Winberry, J. P., and S. Anandakrishnan (2003), Seismicity and neotectonics of West Antarctica, *Geophys. Res. Lett.*, *30*(18), 1931, doi:10.1029/2003GL018001.

X. Chen, H. A. Fricker, P. M. Shearer, and F. Walter, Scripps Institution of Oceanography, University of California, San Diego, La Jolla, CA 92093, USA. (xic002@ucsd.edu)